

---

This is an electronic reprint of the original article.  
This reprint may differ from the original in pagination and typographic detail.

Nilsén, Frans; Flores Ituarte, Inigo; Salmi, Mika; Partanen, Jouni; Hannula, Simo-Pekka  
**Effect of process parameters on non-modulated Ni-Mn-Ga alloy manufactured using powder bed fusion**

*Published in:*  
Additive Manufacturing

*DOI:*  
[10.1016/j.addma.2019.05.029](https://doi.org/10.1016/j.addma.2019.05.029)

Published: 01/08/2019

*Document Version*  
Publisher's PDF, also known as Version of record

*Published under the following license:*  
CC BY

*Please cite the original version:*  
Nilsén, F., Flores Ituarte, I., Salmi, M., Partanen, J., & Hannula, S.-P. (2019). Effect of process parameters on non-modulated Ni-Mn-Ga alloy manufactured using powder bed fusion. *Additive Manufacturing*, 28, 464-474. <https://doi.org/10.1016/j.addma.2019.05.029>

---

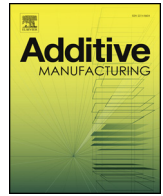
This material is protected by copyright and other intellectual property rights, and duplication or sale of all or part of any of the repository collections is not permitted, except that material may be duplicated by you for your research use or educational purposes in electronic or print form. You must obtain permission for any other use. Electronic or print copies may not be offered, whether for sale or otherwise to anyone who is not an authorised user.



ELSEVIER

Contents lists available at ScienceDirect

## Additive Manufacturing

journal homepage: [www.elsevier.com/locate/addma](http://www.elsevier.com/locate/addma)

Full Length Article

## Effect of process parameters on non-modulated Ni-Mn-Ga alloy manufactured using powder bed fusion

Frans Nilsén<sup>a,b,\*</sup>, Iñigo Flores Ituarte<sup>c</sup>, Mika Salmi<sup>d</sup>, Jouni Partanen<sup>d</sup>, Simo-Pekka Hannula<sup>a</sup><sup>a</sup> Aalto University, Department of Chemistry and Materials Science, Kemistintie 1, 02150, Espoo, Finland<sup>b</sup> Institute of Physics, Czech Academy of Sciences, Na Slovance 1999/2, 182 21, Prague 8, Czech Republic<sup>c</sup> Aalborg University, Department of Materials and Production, A.C. Meyers Vænge 15, 2450 Copenhagen, Denmark<sup>d</sup> Aalto University, Department of Mechanical Engineering, Puumiehenkuja 5, 02150, Espoo, Finland

## ARTICLE INFO

## Keywords:

Direct laser sintering

Laser melting

Additive manufacturing

Magnetic shape memory materials

Magnetic properties

## ABSTRACT

Increasingly, metal parts made by additive manufacturing are produced using powder bed fusion (PBF). In this paper we report upon the combined effects of PBF parameters, including power and scan speed, in layer-by-layer manufacturing of gas atomized non-modulated (NM) Ni-Mn-Ga alloy. The effects of process parameters upon PBF is studied by applying nine different parameter sets in the as-printed state and after homogenization and ordering. The chemical composition of the samples is analyzed using EDX attached to an SEM, and the crystal structures are determined by X-ray diffraction. The phase transformation temperatures are measured using a low-field ac susceptibility measurement system and the magnetic properties are measured with a vibrating sample magnetometer (VSM). Before the heat-treatment, all as-printed samples showed paramagnetic behavior with low magnetization and no phase transformations could be observed in the susceptibility measurements. After annealing, the samples recovered the ferromagnetic behavior with comparable magnetization to annealed gas atomized powder. The as-printed samples were composed of a mixture of different crystal structures. However, after annealing the original NM structure with  $a = b = 5.47 \text{ \AA}$  and  $c = 6.66 \text{ \AA}$  with a  $c/a$ -ratio of 1.22 was recovered and crystallographic twins could be observed in an SEM.

## 1. Introduction

Ferromagnetic Ni-Mn-Ga alloys are known for their large, fast and reversible magnetic-field-induced strains (MFIS) [1–3], which are made possible by twin boundary reorientation induced either by a magnetic field and/or external stress [4]. However, the MFIS is highly dependent upon the chemical composition [5], which defines the crystal structure and phase transformation temperatures [6], and also, as a defect-controlled property, depends on how many obstacles such as grain boundaries and other crystal defects the twin boundary movement needs to overcome during straining [7]. The achievable deformation of the different crystal structures can be estimated by using the formula  $\epsilon_0 = (1 - c/a)$ , where  $c$  and  $a$  are the lattice constants for the different martensitic crystal structures 5 M, 7 M and NM [8,9]. For these martensitic structures the maximum deformations are typically around 6% for 5 M [10], 11% for 7 M [9] and 20–22 % for the NM [1,11] martensites. The non-modulated Ni-Mn-Ga is known for its large deformation resulting from twin boundary movement and also possesses the highest twinning stress, 17–25 MPa, as compared to the 0.5–4 MPa

of the 5 M structure and 3–5 MPa of the 7 M structure [12]. Thus, it is extremely suitable for vibration damping applications [13,14] as the energy of vibration can be absorbed by twin boundary movement.

The highest reversible MFISs are found in single crystal structures, but these structures can be challenging to manufacture. In an effort to increase MFIS in polycrystalline structures, research has been made to both reduce constraints created by grain boundaries by manufacturing highly porous foams [15] or composite structures [16,17] with preferred orientation [18]. Manufacturing Ni-Mn-Ga foams requires the use of special casting replication techniques concomitant with directional solidification [18]. However, these techniques can produce structures of only limited sizes or foams with random distribution of pores. In the present study, we use powder bed fusion to manufacture samples from gas atomized Ni-Mn-Ga powder [19] having a non-modulated crystal structure and good flowability [20].

Powder bed fusion (PBF) is one of the most used additive manufacturing (AM) methods for making high quality metals parts for example in aerospace, automotive and medical sectors [21,22]. Since the technology is rather new there are only a few material systems which

\* Corresponding author at: Institute of Physics, Czech Academy of Sciences, Na Slovance 1999/2, 182 21, Prague 8, Czech Republic.

E-mail address: [nilsen@fzu.cz](mailto:nilsen@fzu.cz) (F. Nilsén).

<https://doi.org/10.1016/j.addma.2019.05.029>

Received 12 November 2018; Received in revised form 24 April 2019; Accepted 28 May 2019

Available online 29 May 2019

2214-8604/© 2019 The Authors. Published by Elsevier B.V. This is an open access article under the CC BY license

(<http://creativecommons.org/licenses/by/4.0/>).

have been studied [22,23]. This is especially true for AM manufactured magnetic materials. In AM, parts are built in a layer-by-layer basis and complex geometries can be easily achieved. Process parameters in PBF have a remarkable effect upon the material properties of the final part [24]. For example, the composition of the material can change because of the evaporation of alloying elements, or the density of the parts can be so low that the parts become delicate. Nevertheless, AM is a potential method for producing complex shape components [25] of materials that are challenging in traditional manufacturing or limited by their geometry as the geometry does not significantly effect to the process [26].

As AM manufacturing methods have become more familiar, several attempts to use AM to manufacture Ni-Mn-Ga structures [27–33] and in other magnetocaloric materials [34] have been made. Additionally, the interaction of laser beam and Ni-Mn-Ga has been studied [35,36]. The AM methods that have so far been utilized with MSM have been binder jet printing [27,28,31], direct metal deposition [30,32] or a combination of both methods in the use of elemental inks [29]. So far it has been proved that complex shapes can be produced [29,31,33] using additive manufacturing methods. However, twins spanning grain boundaries have been observed only in a few studies [28–31,33], and only one study has so far reported MFIS [33] and the reported strain was lower than in polycrystalline Ni-Mn-Ga structures [7]. Additionally, in the case of additive manufacturing processes that utilize binders, extra care must be taken during binder removal so that no residual carbonaceous material is present after final sintering [29]. The diffusion of carbon during removal of binder can lead to carbon or oxygen contamination, which is detrimental [37,38] to Ni-Mn-Ga. In many of the previously reported articles the manufacturing process has additionally led to formation of dendritic structures [30,32] and some compositional inhomogeneity [27,32]. Thus, the aim of this paper is to study whether Ni-Mn-Ga structures can be manufactured using the PBF process without changing the chemical composition of the alloy or creating a dendritic structure. The effect of the PBF process parameters is studied by varying the powder, scanning speed and energy density, with the goal of reaching fully dense parts. Once the optimal parameters are ascertained, it will be possible to later manufacture structures with more complex internal morphology.

## 2. Materials and methods

### 2.1. Powder preparation

In the PBF experiments gas atomized powder having a composition of  $\text{Ni}_{49.8}\text{Mn}_{31.2}\text{Ga}_{19.0}$  was used. The composition of the starting powder was measured using Tescan Mira 3 FEG-SEM with an attached Thermo Fisher Scientific UltraDy EDX detector by measuring multiple points from the cross-section of the powder particles. The atomization was carried out at VTT, Finland. The atomizing gas was argon and the atomization temperature was 1310 °C and the pressure was 50 bar, the particle size of the powder was measured using Malvern Mastersizer 3000 and the D50 of the powder was 47.7  $\mu\text{m}$ , the D10 was 17.5  $\mu\text{m}$  and the D90 was 105  $\mu\text{m}$  and the distribution followed the normal distribution as in previous experiments [19] and the measured density of the powder was 7.91  $\text{g}/\text{cm}^3$ , which is higher than the calculated theoretical density of 7.88  $\text{g}/\text{cm}^3$  indicating that there were no micropores [39]. To achieve an even flow of powder during the powder spreading in the PBF, the atomized powder was mechanically sieved [20] to obtain a size fraction from 25  $\mu\text{m}$  to 45  $\mu\text{m}$ . The particle size distribution of the sieved powder was then measured using Malvern Mastersizer 3000 (Fig. 1a) and the resulting D50 was 20.9  $\mu\text{m}$ , D10 was 10.3  $\mu\text{m}$  and the D9 was 39.8  $\mu\text{m}$ . The sieved powder was also inspected with Tescan Mira SEM (Fig. 1b).

### 2.2. Design of experiment for the PBF

Important parameters involved in the PBF process are: the effective laser power ( $P_{\text{eff}}$ ), the laser scan speed ( $v$ ), the laser scan spacing or hatch distance ( $h$ ), and the layer thickness ( $d$ ). The relation between these variables and the energy density ( $E_v$ ), which is defined as the relative applied laser energy per volume of material and is often used to optimize process variables in laser PBF [24], can be calculated using Eq. (1) [40]:

$$E_v = \frac{P_{\text{eff}}}{v * h * d} \quad (1)$$

In addition to the above parameters, scanning strategy influences the outcome of the process [40]. The range of energy density in our design of experiment (DOE) was initially estimated by consulting available literature. Research on laser interaction with materials such as Ni-Ti, Cu-Al-Ni-Mn and Ni-Mn-Ga show that it is necessary to adjust PBF process parameters to find a suitable processing window to achieve the desired density without compromising the material composition. E.g., in an experimental approach to obtain highly dense Ni-Ti material the energy density was varied from 52.08 to 83.33  $\text{J}/\text{mm}^3$  [41] and from 58.48 to 100.25  $\text{J}/\text{mm}^3$  in another study [42]. Additional experimental work shows that the energy density needs to be lower when highly volatile materials are added to the composition. In the case of SMA alloys based on Cu-Al-Ni-Mn, the range of energy density applied was from 36.67 to 49.55  $\text{J}/\text{mm}^3$  [43] due to the high volatility of Mn. Based on the examined process parameters and energy densities of the mentioned studies [41,42], the objective of our DOE was to explore a combination of process parameters that can minimize the change in the chemical composition and especially to avoid the evaporation of manganese, which is a common problem when Ni-Mn-Ga is manufactured or annealed due to the relatively high vapor pressure of manganese in comparison to that of nickel and gallium [44].

Our research on optimal process parameters was influenced to a large extent by earlier cited work on PBF using SMA materials as well as on experimental research using conventional materials, such as 316 L steel and  $\text{AlSi}_{10}\text{Mg}$ , which are the most widely used material in scientific literature as they are commodity materials in industrial applications of PBF. Prior knowledge shows a considerable number of process parameters that affect achievable mechanical and geometrical properties as well as the densification of the material. These include interactions between machine architecture, material, environmental, and process factors [24]. In regard to machine architecture, the type of laser, the optics, the laser spot size, and the temperature distribution in the chamber as well as the material of the build plate, and heating or cooling of the build plate [45] are important. From the material side the quality of the powder and its flowability properties also contribute [46]. Regarding environment, the type of inert gas, humidity and temperature levels are also relevant. Finally, process parameters, such as the laser power, the laser scan speed, the laser scan spacing or hatch distance, and the layer thickness are also significant to achieve the desired effect in terms of final mechanical properties, material characteristics, and densification of the material. Reaching full density in PBF requires balancing laser power, scan speed, beam size, and layer thickness to ensure on one hand complete melting of the layer and on the other hand that the melting does not result in development of a large number of voids due to the keyhole mode mechanism.

Nevertheless, the fact that the bulk of research is performed with commercial PBF systems limits the possibility to evaluate and test multiple combinations, for example by changing the type of laser and optics. As consequence, the experimental work requires to maintain constant certain parameters and focus only in the ones that allow modification. At the same time, ranking the process parameters in order of significance is fundamental to limit the experimental explosion and scope of DOE studies [47] this is especially applicable for new materials at process parameters screening phases. Our strategy in this screening

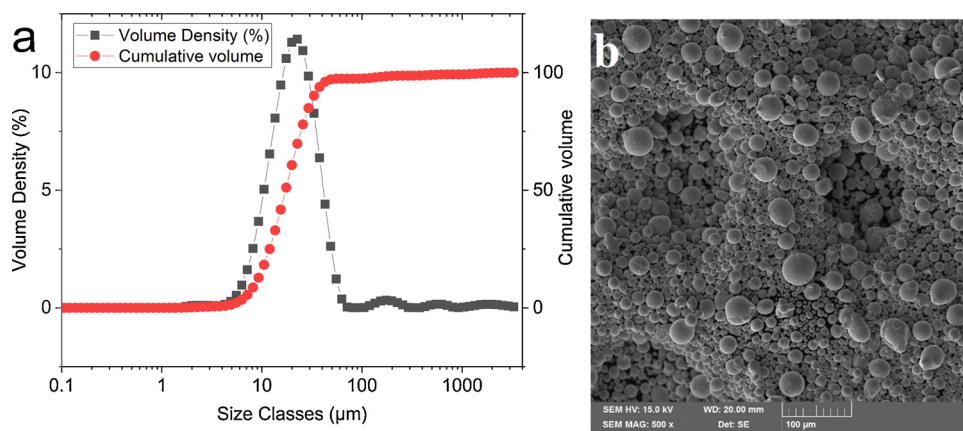


Fig. 1. (a) Particle size distribution of sieved Ni-Mn-Ga powder and (b) scanning electron microscope image of sieved powder at 500x magnification.

DOE was to include the most studied parameters that show higher significant based on prior work, which are power and scanning speed. This allowed us to conduct a high-resolution full factorial DOE. Other experimental approaches include surface response methods (SRM) [48] and nested effects modelling (NEM) techniques [49] which allow more independent variables in the study (e.g. varying condition for layer thickness, hatching strategies and hatching island size) at the cost of experimental resolution.

Table 1 shows the values of the two independent variables of the tested full factorial screening DOE. Power (*P*) and scan speed (*v*) were varied at three discrete levels from 30 to 40 W and 500 to 700 mm/s, respectively. Thus, the *E<sub>v</sub>* region of interest in this study varied from 17.49 and 32.65 J/mm<sup>3</sup>. Other variables, such as layer thickness and scanning strategy were kept constant. The PBF machine used during the experiments was a Mlab Cusing (Concept Laser, Germany) machine with a build envelope of 90 × 90 × 80 mm<sup>3</sup>. The layer thickness was 0.025 mm and the scanning strategy was based on an island exposure of 5 × 5 mm<sup>2</sup> with a track width of 0.14 mm (*W*) and an overlap factor of 0.7 (*A1*) that represents a hatch distance of 98 µm (*W*\**A1*). The laser of the PBF system is an Ytterbium Fiber Laser Model YLM-100-AC with a theoretical maximum power of 100 W, Gaussian distribution with mean wavelength of 1070.15 nm and standard deviation of 0.69 nm, beam diameter (1/*e*<sup>2</sup>) of 54 µm and a maximum scanning speed of 7000 mm/s. The inner protective atmosphere of the build chamber was argon.

The change in material composition is calculated as the percentage of evaporation between the resulted at.% of Mn after PBF on as-built samples as well as heat-treated (HT) samples in relation to the original Mn [at.%]. This percentage of evaporation is used as a performance variable to assess the impact of the process variables on the change in material composition. Thus, the composition of Mn remains the same when this percentage obtains a value of zero. At the same time, the second objective is to obtain as fully dense sample as possible. The result of density measurement is used as another performance indicator.

To perform the experiment, two different types of samples, cuboids and tensile rods, were manufactured for each parameter set. The

cuboids had dimensions of 1 × 1 × 0.5 cm<sup>3</sup>, while the tensile rods had dimensions of *l*<sub>1</sub> of 0.12 cm, *l*<sub>3</sub> of 0.22 cm, *b*<sub>1</sub> of 0.02 cm, *b*<sub>2</sub> of 0.05 cm. The original goal was also to study the mechanical performance of the PBF parts in comparison to process parameters, however, due to the high porosity of the manufactured parts tensile experiments were not possible. As PBF has not been previously used for Ni-Mn-Ga alloys it was unclear how the powder would perform in the process and thus the sintering was performed in two separate sintering runs. During the first round (Fig. 2), only samples with the lowest, average and highest energy densities were printed. After it was clear that the parameters were acceptable, the rest of the samples were sintered during the second round of printing.

The samples were removed from the nickel build plate using a saw and the cuboid samples were subsequently cut in half with an EDM wire saw. For each sample, half of the cuboid was left at the as-sintered stage, while the other half together with the tensile samples were sealed in evacuated crystal ampoules with high vacuum by Finnish Special Glass and heat-treated in Nabertherm Muffle furnace (model L5/12/C6) for homogenization first at 1000 °C for 95 h and then for ordering at 800 °C for 24 h. The heating and cooling rates used were 100 °C/h and the samples were left into furnace to cool into room temperature (e.g. 20 °C). The exact vacuum in the evacuated ampoules was not measured, however, the vacuum was pumped for over 30 min before sealing the ampoule and the expected level was of vacuum was better than 1.33 × 10<sup>-5</sup> Pa, which we have measured previously when making

Table 1  
Powder bed fusion parameters for the nine samples.

Sample #	Power [W]	Scan speed [mm/s]	<i>E<sub>v</sub></i> [J/mm <sup>3</sup> ]
SMA 1	30 (L1)	500 (L1)	24.49
SMA 2	30 (L1)	600 (L2)	20.41
SMA 3	30 (L1)	700 (L3)	17.49
SMA 4	35 (L2)	500 (L1)	28.57
SMA 5	35 (L2)	600 (L2)	23.81
SMA 6	35 (L2)	700 (L3)	20.41
SMA 7	40 (L3)	500 (L1)	32.65
SMA 8	40 (L3)	600 (L2)	27.21
SMA 9	40 (L3)	700 (L3)	23.32

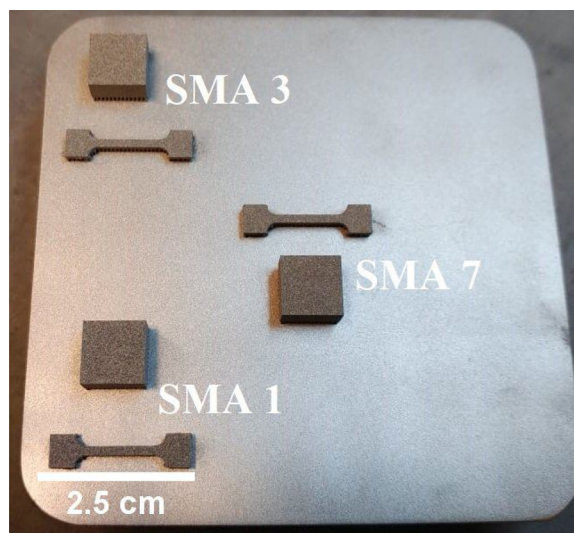


Fig. 2. First powder bed fusion round using highest (SMA 7), medium (SMA 1) and lowest (SMA 3) energy density.

similar heat-treatments in evacuated ampoules [16,19]. The crystal structures were studied using the PANalytical X'Pert Pro XRD and the magnetization of all samples was measured using a laboratory-built VSM applying a NIST nickel disk as a reference sample. The phase transformation temperatures were determined using a laboratory-built low-field *ac* susceptibility measurement device and the densities of samples were measured using the Archimedes method. Finally, the chemical composition was studied using a Tescan Mira 3 FEG-SEM with an attached Thermo Fisher Scientific UltraDry EDX detector, with a Ni-Mn-Ga sample of known composition as a reference, by measuring multiple point and linescans from the ground and polished surfaces of the square samples. The Ni-Mn-Ga sample used as the reference for the standardization was obtained from a trusted source and the composition had been previously confirmed by an XRF dedicated for Ni-Mn-Ga alloys. The standardized EDX analysis is done with NSS microanalysis System - Pathfinder with accelerating voltage at 30 kV and K lines are used for all elements. To ascertain the error in the measurements, the reference material was measured multiple times both before and after standardization. Additionally, before the measurement the samples were left inside the sample chamber for 30 min to give the beam time to settle and special care was taken to keep the measurement, dead time, measuring distance, voltage and beam current constant with each measurement. Each sample was additionally measured multiple times to get an as accurate average chemical composition. The results from density and chemical composition measurements were analyzed in an ANOVA test to study the main effect and interactions of laser power and scanning speed as well as the heat treatment.

### 3. Results and discussion

When the samples were cut from the nickel build plate, it was clear that the samples had not sintered fully during the PBF as some of the samples delaminated easily when samples were handled. The Archimedes density measurements (Table 2) confirmed that the average density of the samples was only 91.4%. As there were no problems in the spreading of the powder during the PBF process given the spherical nature of the gas atomized powder [20], it was concluded that the low density was likely due to the process parameters. Part of the porosity can be also due to so-called gas porosity, which is a known problem in additive powder bed methods [50] and in the SEM studies small round pores were observed in the heat-treated samples. This porosity forms as the argon gas that surrounds the powder particles is trapped inside the melt pool during the melting process due to insufficient overlap of the melt tracks [50]. Another reason for the decrease in the porosity is likely the pore coarsening [51,52] that occurred during the heat-treatment, which was designed for chemical homogenization and ordering but not for the sintering of the samples. As the heat-treatment procedure was same for all samples, this would explain the similar densities after the heat-treatment compared to the densities in the as-printed samples. Thus, it is likely that the reduced density, after

annealing, is due to the combined effect of both gas porosity and pore coarsening. To stop similar decrease in density in the future, the effect of pore coarsening must be taken into effect while designing the heat-treatment procedure [51,52]. To stop water from entering the pores, the samples that showed the highest porosity in the SEM examination, e.g. SMA 2, SMA 3, SMA 5 and SMA 6, were lightly coated with beeswax before immersion for accurate density results. The small change in the chemical composition in comparison to the starting powder can be attributed to the manganese evaporation during heat-treatment, which was performed in vacuum instead of Argon atmosphere. However, this small change is still within the typical manganese loss that can occur during heat-treatment of Ni-Mn-Ga [53].

Fig. 3 presents the calculated main effect on sample density as-printed and after heat-treatment per level of P and v process parameters. The difference between the largest mean minus the smallest mean per factor and per level implies a higher significance of the process parameter over the response. In this regard, P has a slightly higher effect than v when measuring the density as-printed, whereas, this effect is reversed when the heat-treatment is applied, making the effect of v more significant. Both figures display a strong interaction between P and v, therefore the interaction between them and non-linear second order effects are significant on the achievable part density. The results after heat-treatment in Fig. 3b show that while increasing v has a negative effect on part density, increasing the P level creates a denser structure.

Next we considered the material composition and the effect of P and v on percentage of Mn evaporation during the PBF process as well as after heat-treatment. Table 3 shows the chemical composition of the samples obtained by EDX using a reference Ni-Mn-Ga sample. The results displayed show the material composition of all 9 samples as-printed as well as after further the heat-treatment. Fig. 4 shows the average main effect on percentage of Mn evaporation of as-printed and after further heat-treatment per level of P and v process parameters. Again, the difference between the largest mean minus the smallest mean per process parameter and per level on the main effect plot implies a higher significance of the process parameter over the response part density as-printed and after heat-treatment. In this case, due to the strong interaction between P and v the differences are minimal, thus both process parameters show equal significance. Nevertheless, the trend shows that in the case of as-printed samples, the higher the P the larger the evaporation of Mn whereas v has an opposite effect. At a fixed scan speed, higher power implies larger energy density levels thus the evaporation of Mn is higher.

The results after heat-treatment in Table 3 and Fig. 4b show that the chemical composition has been maintained to a large extent and the average Mn evaporation is about 1.6% with a standard deviation of 0.005 in relation to the initial Mn at.% of 31.21. This is promising, as previously manufactured AM samples [27,30,32] have shown that the fast heating and cooling in the AM processes can lead to dendrite growth and chemical inhomogeneity. The chemical composition

**Table 2**

Chemical composition of the as-printed and the heat-treated samples measured with EDX, with the standard deviation used as the error, and Archimedes density measurement results of the samples as-printed and after further heat-treatment.

Sample #	As-printed				Heat-treated			
	Ni [at.%]	Mn [at.%]	Ga [at.%]	Density [%]	Ni [at.%]	Mn [at.%]	Ga [at.%]	Density [%]
SMA 1	50.1 ± 0.04	31.1 ± 0.12	18.9 ± 0.11	88.5 ± 0.57	50.4 ± 0.20	30.6 ± 0.09	19.0 ± 0.23	89.6 ± 0.56
SMA 2	50.2 ± 0.18	30.9 ± 0.13	18.9 ± 0.23	91.6 ± 0.55	50.4 ± 0.14	30.7 ± 0.12	18.9 ± 0.14	78.8 ± 0.64
SMA 3	50.1 ± 0.33	31.1 ± 0.43	18.8 ± 0.11	90.4 ± 0.55	50.6 ± 0.19	30.7 ± 0.14	18.8 ± 0.15	75.2 ± 0.67
SMA 4	50.4 ± 0.36	30.7 ± 0.28	18.9 ± 0.39	92.9 ± 0.54	50.4 ± 0.29	30.6 ± 0.25	19.0 ± 0.33	84.1 ± 0.60
SMA 5	50.2 ± 0.18	30.9 ± 0.09	18.9 ± 0.14	91.6 ± 0.55	50.7 ± 0.12	30.6 ± 0.06	18.7 ± 0.14	82.6 ± 0.61
SMA 6	50.3 ± 0.11	31.0 ± 0.17	18.8 ± 0.15	91.6 ± 0.55	50.5 ± 0.09	30.9 ± 0.09	18.6 ± 0.10	80.5 ± 0.62
SMA 7	50.3 ± 0.17	30.9 ± 0.15	18.9 ± 0.16	91.0 ± 0.55	50.6 ± 0.17	30.8 ± 0.19	18.5 ± 0.22	87.1 ± 0.58
SMA 8	50.3 ± 0.09	30.8 ± 0.21	18.9 ± 0.21	92.8 ± 0.54	50.5 ± 0.15	30.6 ± 0.06	19.0 ± 0.11	85.2 ± 0.59
SMA 9	50.3 ± 0.15	31.0 ± 0.16	18.7 ± 0.07	92.1 ± 0.54	50.6 ± 0.12	30.6 ± 0.09	18.8 ± 0.08	84.9 ± 0.59

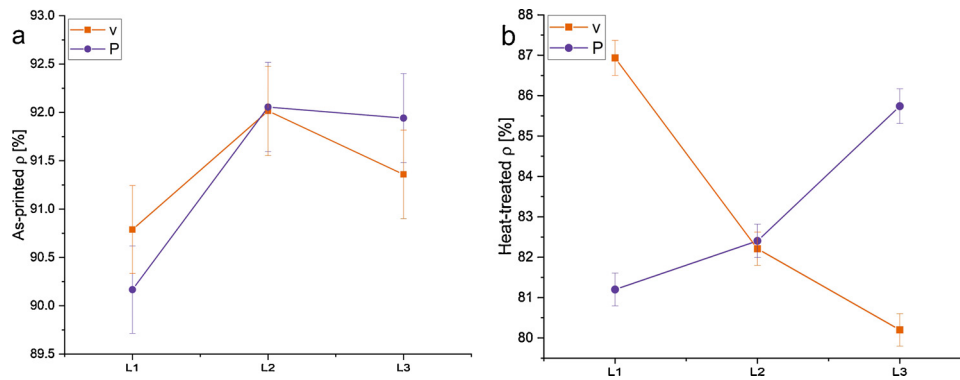


Fig. 3. Plot of the main effects of power (P) and scan speed (v) on sample density as-printed (a) and after heat-treatment (b) with L1, L2 and L3 representing the combinations of low, medium and high power (P) and scanning speed (v) respectively as shown in Table 1, with error bars from propagated error of the scale.

analysis using EDX revealed that the PBF process and the following heat-treatment led only to a small compositional change from the starting composition of powder. Based on the change in the chemical composition, both the scanning speed and power have comparable effects as higher power increases manganese evaporation, while increasing the speed reduces it. For example, if the amount of manganese in SMA 7 is compared to SMA 3 there is approximately 0.3 at.% less manganese in SMA 7. A similar trend can be also seen with other samples, which have comparable energy densities such as SMA 4 and SMA 8.

To explore further the effect and significance of first order, second order, and interaction terms, an ANOVA test was performed. Table 3 evaluates quantitatively the significance of the process parameter terms as well as the impact of the heat treatment (HT) in the densification of the samples. Simultaneously, the percentage of Mn evaporation response of the process is also analyzed. In the ANOVA test, the continuous predictors (i.e. P and v) and one categorical predictor (i.e. the effect of HT) were included and a backward elimination of terms was applied. Initially, all potential first order, second order and interaction terms were included in the model and the least significant term were removed at each step. The algorithm stops when all the terms in the model have P-values that are lower or equal to 0.1. Thus, second order and interaction terms with higher P-value than 0.1 are removed from the regression model. For terms with P-value < 0.1 the difference between the means are statistically significant.

For both responses, the effect of the HT has more significance when compared with process parameters P and v. In the case of the densification of the SMA powder, the significance of the HT treatment (P = 0.004) is notably higher in comparison to process parameters P

(P = 0.303) and v (P = 0.345). In addition, quadratic terms and interaction terms between HT, P and v show also high statistical significance. In the case of percentage of Mn evaporation, the significance of HT is even higher (P = 0), but in this case process parameter have stronger influence P (P = 0.063) and v (P = 0.074) in the evaporation of Mn during the PBF process. Similarly, quadratic terms and interaction term between P and v show high statistical significance. However, the interaction terms between P, v and HT were excluded from the model due to lower significance with P-value > 0.1.

Table 4 shows the regression equations after HT for [%] density and [%] Mn evaporation as function of process parameters P and v. At the same time, the results for the model summary are displayed to determine how well the regression equation fits the data. In the case of densification process, we compare the [%] density achieved during the AM process and the HT of the SMA samples. The model summary shows good results with a high R<sup>2</sup> = 97.9%, low standard error of the regression S = 1.387 and the ability to predict the response for new observation of R<sup>2</sup>(pred.) = 76.58%. On the contrary, regarding the percentage of Mn evaporation during the same process the percentage of variation drops to R<sup>2</sup> = 76.22%, standard error of the regression S = 0.003 and the ability to predict the response for new observation of R<sup>2</sup>(pred.) = 20.45%.

In summary, both multivariable regression equations have good fit with the existing data and they were used to define optimal process parameter regarding the fabrication of SMA (i.e. gas atomized non-modulated Ni-Mn-Ga alloy) using PBF layer-by-layer manufacturing. Fig. 5 shows the contour plots for [%] Density and [%] Mn evaporation based on the presented regression equations. At first glance can be seen that low P and high v values are responsible for reduced [%] density of

Table 3

ANOVA table for [%] Density and [%] Mn evaporation including P and v as continuous predictors and HT as a categorical predictor.

Source	[%] Density					[%] Mn evaporation				
	DF	Adj SS	Adj MS	F-Value	P-Value	DF	Adj SS	Adj MS	F-Value	P-Value
Regression	11	537,918	489,017	25.43	0	6	0.000411	0.000068	5.88	0.006
P	1	2,438	24,384	1.27	0.303	1	0.00005	0.00005	4.28	0.063
V	1	2,018	20,183	1.05	0.345	1	0.000045	0.000045	3.9	0.074
HT	1	39,362	393,618	20.47	0.004	1	0.00032	0.00032	27.51	0
P <sup>2</sup>	1	2,004	20,041	1.04	0.347	1	0.000051	0.000051	4.37	0.061
V <sup>2</sup>	1	1,772	17,716	0.92	0.374	1	–	–	–	–
P*v	1	0.177	0.1773	0.09	0.772	1	0.000048	0.000048	4.08	0.068
P*HT	1	21,727	217,271	11.3	0.015	–	–	–	–	–
V*HT	1	23,234	232,340	12.08	0.013	–	–	–	–	–
P <sup>2</sup>	1	12,169	121,686	6.33	0.046	–	–	–	–	–
P*v*HT	1	24,175	241,749	12.57	0.012	–	–	–	–	–
P <sup>2</sup> *v	–	–	–	–	–	1	0.000049	0.000049	4.21	0.065
V <sup>2</sup> *HT	1	8,160	81,603	4.24	0.085	–	–	–	–	–
Error	6	11,537	19,228	–	–	11	0.000128	0.000012	–	–
Total	17	549,455	–	–	–	17	0.000539	–	–	–

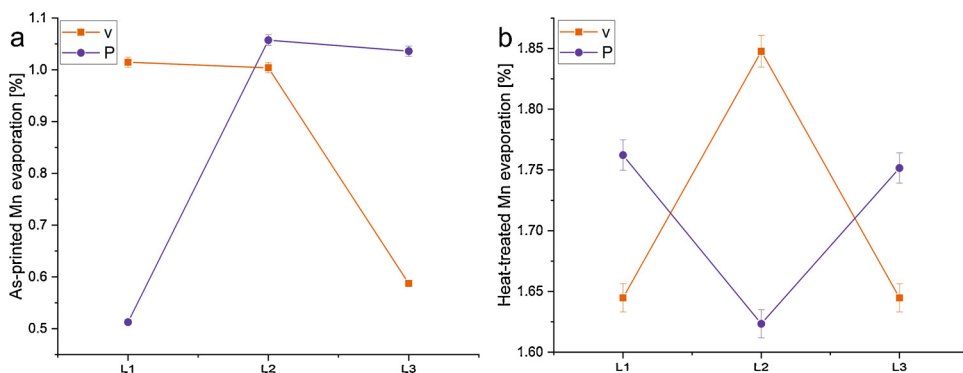


Fig. 4. Plot of the main effects of power (P) and scan speed (v) on percentage of evaporation of Mn [at.%] of as-printed samples (a) and after further heat-treatment (b) with L1, L2 and L3 representing the combinations of low, medium and high power (P) and scanning speed (v) respectively as shown in Table 1, with error bars calculated from the propagated error from EDX standard deviation divided by the amount of measurement points.

the samples (density < 75%). Similarly, the [%] of Mn evaporation is lower when P and v are at the lowest and highest level, respectively (Mn evaporation < 1.4%). To this end, low laser power (P) and high scan speed (v) implies lower energy density.

The highest density of the SMA samples (density > 87.5%) is obtained when the P is at maximum level and the v is at the lowest, which implies the highest energy density used during the DOE. However, as a general trend, this increased density is achieved at the cost of [%] Mn evaporation (Mn evaporation > 2.0%). The experimental work and regression equations shows a tradeoff between objectives. Therefore, process parameters need to be carefully formulated to have the ability to produce Ni-Mn-Ga components with increased density without penalties in material composition.

If we take a closer look to Fig. 5 and the region of maximum [%] Mn evaporation. The contour plot, based on the results of the multivariable regression, shows a region of maximum [%] Mn evaporation > 2.0%, when the P is within the range of 32.2 W and 38 W and the v is within the range of 500 mm/sec and 535 mm/sec, thus a region of higher energy density. On the contrary, the region of minimum [%] Mn evaporation < 1.4% is within the range of 31.5 W and 35.5 W and the v is within the range of 680 mm/sec and 700 mm/sec, thus a region of lower energy density in comparison.

The aforementioned tradeoff between achievable [%] density and [%] Mn evaporation can be understood further by looking at Fig. 6. The horizontal axis shows the tested energy densities ( $E_v$ ), while the vertical axis on the left hand side shows the [%] Mn evaporation, and the vertical axis on the right/hand side shows the achieved part [%] density after the samples were heat-treated. If we simplify the overall trend using a linear fit, Fig. 6 shows how the part density increases at higher energy density levels at the cost of Mn evaporation. However, in the case of the Mn evaporation non-linear effects between  $P \cdot v$  are more significant (P-value = 0.068) as well as the second order interaction  $P^2 \cdot v$  (P-value = 0.065), which explains the irregular trend in [%] Mn evaporation. It should be noted that, the resulting percentage of variation of regression model drops from  $R^2 = 97.9\%$  of [%] density to  $R^2 = 76.22\%$  of [%] Mn evaporation. Therefore, we can deduce that modelling the changes in material composition is more complex in comparison to the densification. Future experiments are planned to account for a larger energy density range that can help to model the change in material composition, additionally it will be necessary to include the process uncertainty by including experimental and measurement repetitions in a more systematic way.

Overall, after these initial set of experiments, it should be

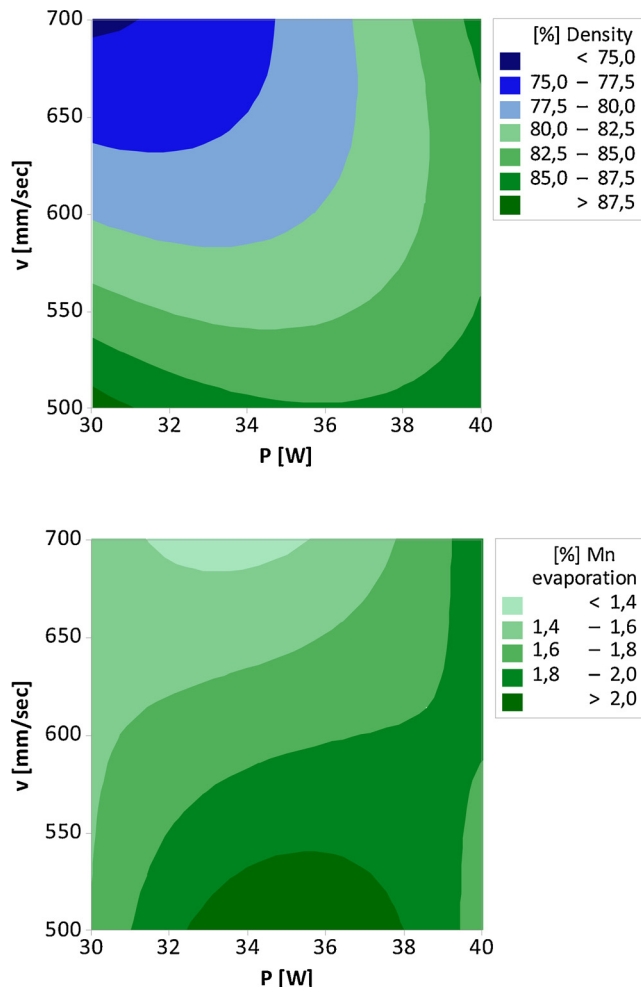


Fig. 5. Contour plots for [%] Density and [%] Mn evaporation based on the regression models of HT samples.

mentioned that the evaporation of Mn has been maintained very low with no large change in the chemical composition. At the same time, the density of all the samples was relatively low which led to the breaking of tensile rods during sample preparation. However, once the

Table 4

Multivariable regression equations for [%] Density and [%] Mn evaporation including P and v terms after HT process.

S	R <sup>2</sup>	R <sup>2</sup> (pred.)	Regression equation
1,387	97.90%	76.58%	$[\%] \rho = 413.6 - 10.42P - 0.496v + 0.0995P^2 + 0.000192V^2 + 0.00653P \cdot v$
0.003	76.22%	20.45%	$[\%] Mn = -122.9 + 7.33P + 0.2v - 0.106P^2 - 0.118P \cdot v + 0.000171P^2 \cdot v$

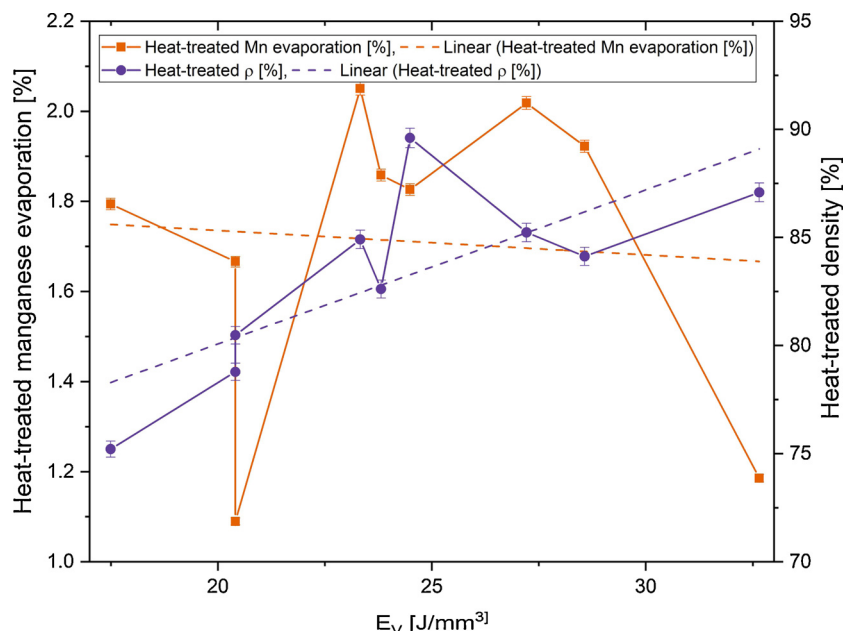


Fig. 6. Evaporation of Mn and part density after heat-treatment in relation to energy density on PBF.

correct manufacturing parameters are found, more complex internal structures can be designed with controlled porosity to achieve high strains, since grain boundaries can act as pinning sites for the twin boundary movement [31,33].

Apart from the ANOVA test and statistical analysis of the process conditions, the X-ray diffraction measurements of the as-sintered samples showed that the crystal structure was composed of a mixture of different structures (Fig. 7a). The intensity of the measured spectra changed according to the density of samples (Table 2) SMA 8 having the highest intensity. However, the heat-treatment recovered the original non-modulated martensitic crystal structure (Fig. 7b) and the crystal parameters were  $a = b = 5.47 \text{ \AA}$  and  $c = 6.66 \text{ \AA}$  while the calculated  $c/a$ -ratio was 1.22.

As the heating and cooling occurs rapidly during the process, it was expected that some inhomogeneity and thermal stresses would form during the process. It is likely that this could be diminished by using a heated powder bed as it is known to reduce the formation of stresses and increase density of PBF parts [54]. A similar effect has been seen in the previously produced AM parts in the as-printed structures [30] with the main difference being that in samples manufactured using the binder-jet method [28,31,33] the homogenization and ordering can occur during the sintering treatment of the sample. However, as no binders containing carbon and oxygen [27] are needed in PBF, the risk of contamination during the heat-treatment process is lower.

When the heat-treated samples were studied using scanning electron microscopy, the pores created by the gas bubbles showed up as spherical pores. The SEM images also revealed twin structures in the bottom of the unpolished pore-plateaus (Fig. 8) and twins could be observed clearly in SMA 2, SMA 4, SMA 8 and SMA 9 samples, which all had large open pore structures. Similarly to previous Ni-Mn-Ga structures manufactured using AM methods, the twins go across the visible grain boundaries [29,31,33]. This is promising, as it can indicate the sintered boundaries are not necessarily a hindrance to the twin boundary movement [29]. Additionally, the PBF did not produce a dendritic cooling structure which occurred in previously reported studies [30,32]. Based on the SEM examination, the scanning speed has a higher effect on the formation on large pores than the power in the PBF process as the samples that were printed at higher speeds have larger pores, while the pores in SMA 1, SMA 4 and SMA 7 are smaller.

Even though there was no apparent change in the chemical composition the magnetic measurements indicated that the as-printed powder was paramagnetic (Fig. 9a) and no phase transformation could be observed in the low-field ac susceptibility measurements. This is likely due to chemical inhomogeneity and internal stresses due to the fast cooling in the PBF process. The subsequent homogenization and ordering heat-treatment recovered the ferromagnetic properties of the alloy (Fig. 9b). A similar effect has been previously observed when magnetic properties of the as-atomized Ni-Mn-Ga powder are compared

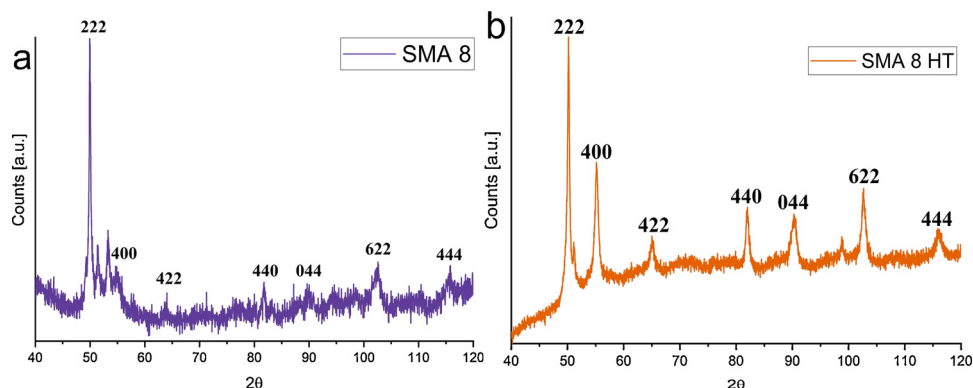
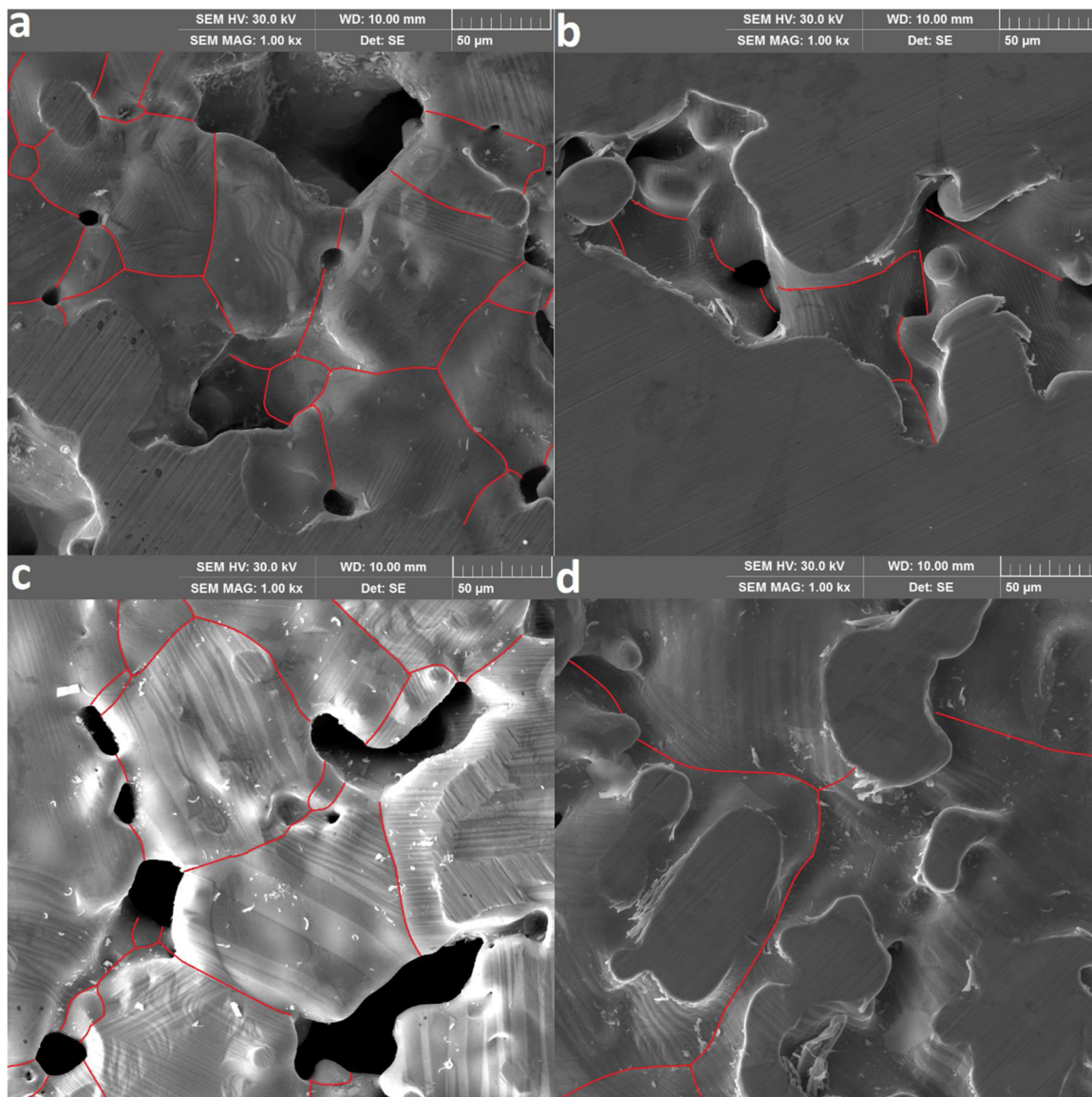
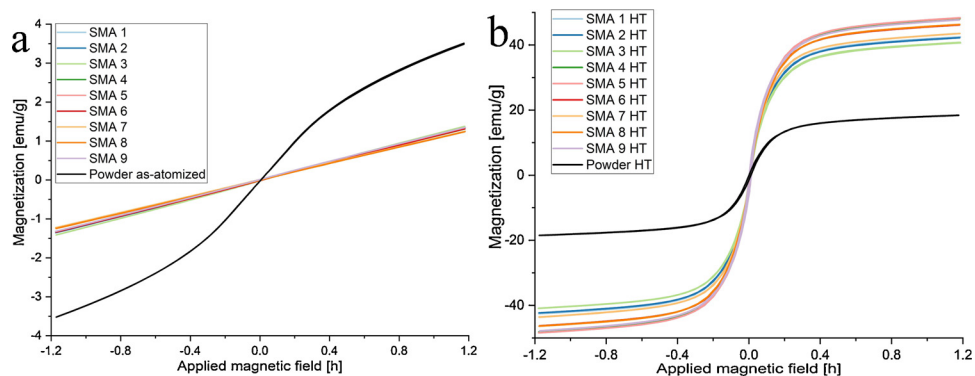


Fig. 7. XRD measurements of PBF sample 8: a) before heat-treatment and b) after heat-treatment with some identified peaks.



**Fig. 8.** Scanning electron microscopy images of: a) SMA 2, b) SMA 4, c) SMA 8 and d) SMA 9 at 1000x magnification of large unground pore-plateau showing twins, the small white particles are contaminations created when sample was removed from quartz ampoule. The grain boundaries are marked with a red line in the images to make them more visible. (For interpretation of the references to colour in this figure legend, the reader is referred to the web version of this article).



**Fig. 9.** Vibrating sample magnetometer measurements of the: (a) as-printed samples and as-atomized powder and (b) homogenized and ordered samples and powder heat-treated using the salt-method [17] at 760 °C for 24 h.

**Table 5**  
Phase transformation temperatures of heat-treated powder and heat-treated PBF samples measuring using laboratory built low-field ac susceptibility measuring system.

	$M_s$ [°C]	$M_f$ [°C]	$A_s$ [°C]	$A_f$ [°C]	Curie [°C]
Powder HT	59	50	51	60	66
SMA 1	74	68	71	75	96
SMA 2	73	68	71	75	95
SMA 3	70	65	68	71	92
SMA 4	73	68	71	74	95
SMA 5	73	68	71	75	95
SMA 6	72	66	69	73	94
SMA 7	68	62	65	70	91
SMA 8	73	68	70	74	94
SMA 9	69	63	66	70	92

to heat-treated powder [19]. If the magnetization of the heat-treated powder and sintered samples are compared, the sintered samples have higher magnetization likely due to being solid and as they have larger grain size than the powder particles. Additionally, the longer heat-treatment at a higher temperature can have led to a higher degree of ordering and chemical homogenization. If the measured magnetization is compared to the literature reference values between 35–55 emu/g [1,55] in NM, the highest saturation magnetization found in SMA 9 is 46.3 emu/g is well inside this range.

As the as-printed samples were paramagnetic (Fig. 9a) no phase transformation temperatures could be measured with ac susceptibility. However, after the heat-treatment the phase transformation temperatures could be measured without difficulty (Table 5). Compared to the phase transformation temperatures of the heat-treated atomized powder, the phase transformation in the PBF samples occurred at temperatures that are approximately 10–20 degrees higher. As it is known [56–59], the atomic ordering of the  $L2_1$  structure affects the properties of the structure since the ordering of the parent phase is inherited during the martensitic transformation. The effect of increased ordering can be typically observed by the elevated Curie and martensitic transformation temperatures [56–59]. As the heat-treatment procedure for the PBF parts included both homogenization at 1000 °C and ordering treatment at 800 °C, it is likely that the PBF parts have a fully homogenized and ordered structure. In addition to the effect of increased atomic order, the change in the transformation temperatures is also partly due to the change in the chemical composition during heat-treatment.

In order to make a preliminary selection of process parameters for further experimental work, a comparison between the contour plots in Fig. 5 and the results of the vibrating sample magnetometer measurements is required. The results of the magnetometer show that all the samples maintained magnetic properties between 35 to 55 emu/g; therefore, all the combinations of P and v were able to create samples of non-modulated Ni-Mn-Ga with magnetic properties. In this DOE, the [%] Mn evaporation is within the acceptable range, making more relevant the objective of obtaining higher [%] density of the manufactured samples. Consequently, future experimental work is planned to test at wider range of energy density starting from 28 J/mm<sup>3</sup> to 40 J/mm<sup>3</sup>.

#### 4. Conclusions

We have demonstrated that PBF can be used to manufacture Ni-Mn-Ga structures using the gas atomized powder. The as-sintered samples were paramagnetic likely because of internal strains, chemical inhomogeneity and atomic disorder related to the fast heating and cooling in the sintering process. However, the following heat-treatment procedure homogenized and ordered the structure and recovered the original non-modulated structure and the magnetic properties. Also no dendritic cooling structures were found in the SEM images.

The results of the DOE, ANOVA study and multivariable regression analysis shows that there is general a tradeoff between increasing the [%] density of the samples at the cost of increasing the [%] Mn evaporation. At the same time, the results of the ANOVA test show that the heat-treatment has a major significance in the modification of material composition as well as on the densification of the material. In addition, the determination of the optimal process parameters is paramount, especially when accounting for second order and interaction effects. As consequence, process parameters, as well as material composition needs to be carefully formulated to have the ability to produce Ni-Mn-Ga components with increased density without penalties in material composition.

Future experiments are planned with increased  $E_v$  to study the possibility to produce fully dense samples and to statistically model the densification process, and therefore to obtain an operational formula for the porosity level of the material as a function of the process parameters with a larger energy range. Similarly, future experiments will require to study the changes in material composition specially in relation to [%] Mn evaporation in order to maintain magnetic properties intact. Additionally, in the future experiments, we plan to replace the Archimedes method by Gas pycnometry to measure the porosity level of the obtained samples. Ideally, the densification of the material can be also evaluated by computer tomography [60] to understand the size and distribution of porosity across the samples and determine its morphology and whether is layered porosity or interconnected porosity across layers. The results of this study show that the modelling of changes in material composition is more complex in comparison to the densification and possibly more sensitive to outliers as well as the uncertainty in the experimental work. Consequently, in order to create a robust model of the relationship between input and output parameters future experiment are planned to account systematically for (i) the experimental uncertainty, thus including several repetitions per experimental combination and to account the possible variability during the heat treatment process as well as (ii) the measurement uncertainty.

In summary, this initial work shows that twins were observed by SEM on the unground surfaces of the annealed samples and that no large compositional heterogeneity could be observed in the sample as such the PBP shows promise as a suitable way to process Ni-Mn-Ga alloys. Additionally, as twins spanned some of the resulting grain boundaries, it is likely that the boundaries will not hinder twin boundary movement in samples manufactured with PBF. Thus the complex geometry afforded by computer aided design could be utilized with PBF to manufacture customized vibration damping elements from the non-modulated Ni-Mn-Ga. Additionally, the results show that PBF is suitable for producing complex shapes from Ni-Mn-Ga alloys, such as the tensile rods, which opens the possibility of manufacturing actuators with complex external and internal geometries, that can be used to reduced grain boundary constraints, while retaining chemical homogeneity.

#### Acknowledgements

We gratefully acknowledge the support of the Aalto University seed funding for the DEMINFUN-project (974110). Frans Nilsén also acknowledges (in part) support by Operational Program Research, Development and Education financed by European Structural and Investment Funds and the Czech Ministry of Education, Youth and Sports (Project No. SOLID21 - CZ.02.1.01/0.0/0.0/16\_019/0000760).

#### References

- [1] C.B. Jiang, T. Liang, H.B. Xu, M. Zhang, G.H. Wu, Superhigh strains by variant reorientation in the nonmodulated ferromagnetic NiMnGa alloys, *Appl. Phys. Lett.* 81 (2002) 2818–2820, <https://doi.org/10.1063/1.1512948>.
- [2] I. Aaltio, M. Lahelin, O. Söderberg, O. Heczko, B. Löfgren, Y. Ge, J. Seppälä, S.-P. Hannula, Temperature dependence of the damping properties of Ni–Mn–Ga alloys, *Mater. Sci. Eng. A* 481–482 (2008) 314–317, <https://doi.org/10.1016/j.msea.>

- 2006.12.229.
- [3] K.H.J. Buschow (Ed.), *Encyclopedia of Materials: Science and Technology*, Elsevier, Amsterdam; New York, 2001.
- [4] N. Okamoto, T. Fukuda, T. Kakeshita, Magnetocrystalline anisotropy and twinning stress in Ni-Mn-Ga ferromagnetic shape memory alloys, *J. Phys. Conf. Ser.* 51 (2006) 315–318, <https://doi.org/10.1088/1742-6596/51/1/073>.
- [5] X. Jin, M. Marioni, D. Bono, S.M. Allen, R.C. O'Handley, T.Y. Hsu, Empirical mapping of Ni-Mn-Ga properties with composition and valence electron concentration, *J. Appl. Phys.* 91 (2002) 8222, <https://doi.org/10.1063/1.1453943>.
- [6] J. Pons, V.A. Chernenko, R. Santamarta, E. Cesari, Crystal structure of martensitic phases in Ni-Mn-Ga shape memory alloys, *Acta Mater.* 48 (2000) 3027–3038.
- [7] U. Gaitzsch, M. Pötschke, S. Roth, B. Rellinghaus, L. Schultz, A 1% magnetostrain in polycrystalline 5M Ni-Mn-Ga, *Acta Mater.* 57 (2009) 365–370, <https://doi.org/10.1016/j.actamat.2008.09.017>.
- [8] P. Müllner, V.A. Chernenko, G. Kostorz, Large cyclic magnetic-field-induced deformation in orthorhombic (14M) Ni-Mn-Ga martensite, *J. Appl. Phys.* 95 (2004) 1531–1536, <https://doi.org/10.1063/1.1639144>.
- [9] A. Sozinov, A.A. Likhachev, N. Lanska, K. Ullakko, Giant magnetic-field-induced strain in NiMnGa seven-layered martensitic phase, *Appl. Phys. Lett.* 80 (2002) 1746–1748, <https://doi.org/10.1063/1.1458075>.
- [10] S.J. Murray, M. Marioni, S.M. Allen, R.C. O'Handley, T.A. Lograsso, 6% magnetic-field-induced strain by twin-boundary motion in ferromagnetic Ni-Mn-Ga, *Appl. Phys. Lett.* 77 (2000) 886, <https://doi.org/10.1063/1.1306635>.
- [11] O. Söderberg, L. Straka, V. Novák, O. Heczko, S.-P. Hannula, V.K. Lindroos, Tensile/compressive behaviour of non-layered tetragonal Ni<sub>52</sub>Mn<sub>25</sub>Co<sub>23</sub> alloy, *Mater. Sci. Eng. A* 386 (2004) 27–33, <https://doi.org/10.1016/j.msea.2004.07.045>.
- [12] O. Heczko, L. Straka, K. Ullakko, Relation between structure, magnetization process and magnetic shape memory effect of various martensites occurring in Ni-Mn-Ga alloys, *J. Phys. IV* 112 (2003) 959–962, <https://doi.org/10.1051/jp4:20031040>.
- [13] X.W. Liu, O. Söderberg, K. Koho, N. Lanska, Y. Ge, A. Sozinov, V.K. Lindroos, Vibration cavitation behaviour of selected Ni-Mn-Ga alloys, *Wear* 258 (2005) 1364–1371, <https://doi.org/10.1016/j.wear.2004.10.001>.
- [14] I. Aaltio, K.P. Mohanchandra, O. Heczko, M. Lahelin, Y. Ge, G.P. Carman, O. Söderberg, B. Löfgren, J. Seppälä, S.-P. Hannula, Temperature dependence of mechanical damping in Ni-Mn-Ga austenite and non-modulated martensite, *Scr. Mater.* 59 (2008) 550–553, <https://doi.org/10.1016/j.scriptamat.2008.05.005>.
- [15] M. Chmielus, X.X. Zhang, C. Witherspoon, D.C. Dunand, P. Müllner, Giant magnetic-field-induced strains in polycrystalline Ni-Mn-Ga foams, *Nat. Mater.* 8 (2009) 863–866, <https://doi.org/10.1038/nmat2527>.
- [16] F. Nilsén, J. Lehtonen, Y. Ge, I. Aaltio, S.-P. Hannula, Highly porous spark plasma sintered Ni-Mn-Ga structures, *Scr. Mater.* 139 (2017) 148–151, <https://doi.org/10.1016/j.scriptamat.2017.06.040>.
- [17] F. Nilsén, I. Aaltio, S.-P. Hannula, Comparison of magnetic field controlled damping properties of single crystal Ni-Mn-Ga and Ni-Mn-Ga polymer hybrid composite structures, *Compos. Sci. Technol.* 160 (2018) 138–144, <https://doi.org/10.1016/j.compscitech.2018.03.026>.
- [18] P. Zheng, N.J. Kucza, Z. Wang, P. Müllner, D.C. Dunand, Effect of directional solidification on texture and magnetic-field-induced strain in Ni-Mn-Ga foams with coarse grains, *Acta Mater.* 86 (2015) 95–101.
- [19] F. Nilsén, I. Aaltio, Y. Ge, T. Lindroos, S.P. Hannula, Characterization of gas atomized Ni-Mn-Ga powders, *Mater. Today Proc.* 2 (2015) S879–S882.
- [20] S. Berretta, O. Ghita, K. Evans, A. Anderson, C. Newman, Size, shape and flow of powders for use in selective laser sintering (SLS), in: P. da Silva Bártolo, A. de Lemos, A. Pereira, A. Mateus, C. Ramos, C. Santos, D. Oliveira, E. Pinto, F. Craveiro, H. da Rocha Terreiro Galha Bártolo, H. de Amorim Almeida, I. Sousa, J. Matias, L. Durão, M. Gaspar, N. Fernandes Alves, P. Carreira, T. Ferreira, T. Marques (Eds.), *High Value Manuf. Adv. Res. Virtual Rapid Prototyp.*, CRC Press, 2013, pp. 49–54, <https://doi.org/10.1201/b15961-11>.
- [21] N. Kretschmar, I.F. Ituarte, J. Partanen, A decision support system for the validation of metal powder bed-based additive manufacturing applications, *Int. J. Adv. Manuf. Technol.* 96 (2018) 3679–3690, <https://doi.org/10.1007/s00170-018-1676-8>.
- [22] T.D. Ngo, A. Kashani, G. Imbalzano, K.T.Q. Nguyen, D. Hui, Additive manufacturing (3D printing): a review of materials, methods, applications and challenges, *Compos. Part B Eng.* 143 (2018) 172–196, <https://doi.org/10.1016/j.compositesb.2018.02.012>.
- [23] W.E. Frazier, Metal additive manufacturing: a review, *J. Mater. Eng. Perform.* 23 (2014) 1917–1928, <https://doi.org/10.1007/s11665-014-0958-z>.
- [24] T. DebRoy, H.L. Wei, J.S. Zuback, T. Mukherjee, J.W. Elmer, J.O. Milewski, A.M. Beese, A. Wilson-Heid, A. De, W. Zhang, Additive manufacturing of metallic components – process, structure and properties, *Prog. Mater. Sci.* 92 (2018) 112–224, <https://doi.org/10.1016/j.pmatsci.2017.10.001>.
- [25] I.F. Ituarte, N. Kretschmar, S. Chekurov, J. Partanen, J. Tuomi, Additive Manufacturing Validation Methods, *Technology Transfer Based on Case Studies*, 1st ed., Springer International Publishing, 2019, [https://link.springer.com/chapter/10.1007/978-3-319-76084-1\\_7](https://link.springer.com/chapter/10.1007/978-3-319-76084-1_7).
- [26] D.W. Rosen, Research supporting principles for design for additive manufacturing: this paper provides a comprehensive review on current design principles and strategies for AM, *Virtual Phys. Prototyp.* 9 (2014) 225–232, <https://doi.org/10.1080/17452759.2014.951530>.
- [27] A. Mostafaei, K.A. Kimes, E.L. Stevens, J. Toman, Y.L. Krimer, K. Ullakko, M. Chmielus, Microstructural evolution and magnetic properties of binder jet additive manufactured Ni-Mn-Ga magnetic shape memory alloy foam, *Acta Mater.* 131 (2017) 482–490, <https://doi.org/10.1016/j.actamat.2017.04.010>.
- [28] A. Mostafaei, P. Rodriguez De Vecchis, E.L. Stevens, M. Chmielus, Sintering regimes and resulting microstructure and properties of binder jet 3D printed Ni-Mn-Ga magnetic shape memory alloys, *Acta Mater.* 154 (2018) 355–364, <https://doi.org/10.1016/j.actamat.2018.05.047>.
- [29] S.L. Taylor, R.N. Shah, D.C. Dunand, Ni-Mn-Ga micro-trusses via sintering of 3D-printed inks containing elemental powders, *Acta Mater.* 143 (2018) 20–29, <https://doi.org/10.1016/j.actamat.2017.10.002>.
- [30] J. Toman, P. Müllner, M. Chmielus, Properties of as-deposited and heat-treated Ni-Mn-Ga magnetic shape memory alloy processed by directed energy deposition, *J. Alloys Compd.* 752 (2018) 455–463, <https://doi.org/10.1016/j.jallcom.2018.04.059>.
- [31] M.P. Caputo, C.V. Solomon, A facile method for producing porous parts with complex geometries from ferromagnetic Ni-Mn-Ga shape memory alloys, *Mater. Lett.* 200 (2017) 87–89, <https://doi.org/10.1016/j.matlet.2017.04.112>.
- [32] E. Stevens, J. Toman, K. Kimes, V. Chernenko, A. Wojcik, W. Maziarz, M. Chmielus, Microstructural evaluation of magnetocaloric Ni-Co-Mn-Sn produced by directed energy deposition, *Microsc. Microanal.* 22 (2016) 1774–1775, <https://doi.org/10.1017/S1431927616009715>.
- [33] M.P. Caputo, A.E. Berkowitz, A. Armstrong, P. Müllner, C.V. Solomon, 4D printing of net shape parts made from Ni-Mn-Ga magnetic shape-memory alloys, *Addit. Manuf.* 21 (2018) 579–588, <https://doi.org/10.1016/j.addma.2018.03.028>.
- [34] E. Stevens, K. Kimes, V. Chernenko, P. Lazpita, A. Wojcik, W. Maziarz, M. Chmielus, Direct laser deposition and homogenization of Ni-Co-Mn-Sn magnetocaloric material, *Microsc. Microanal.* 24 (2018) 956–957, <https://doi.org/10.1017/S1431927618005275>.
- [35] C.A. Biffi, A. Tuissi, Fiber laser drilling of Ni46Mn27Ga27 ferromagnetic shape memory alloy, *Opt. Laser Technol.* 63 (2014) 1–7, <https://doi.org/10.1016/j.optlasotec.2014.03.010>.
- [36] C.M. Craciunescu, R.M. Miranda, R.J.C. Silva, E. Assunção, F.M. Braz Fernandes, Laser beam interaction with Ni-Mn-Ga ferromagnetic shape memory alloys, *Opt. Lasers Eng.* 49 (2011) 1289–1293, <https://doi.org/10.1016/j.optlaseng.2011.06.007>.
- [37] D.C. Dunand, P. Müllner, Size effects on magnetic actuation in Ni-Mn-Ga shape-memory alloys, *Adv. Mater.* 23 (2011) 216–222, <https://doi.org/10.1002/adma.201002753>.
- [38] X. Lu, X. Chen, L. Qiu, Z. Qin, Martensitic transformation of Ni-Mn-Ga(C, Si, Ge) heusler alloys, *J. Phys. IV. France.* 112 (2003) 917–920, <https://doi.org/10.1051/jp4:20031030>.
- [39] W.B. Eissen, B.L. Ferguson, R.M. German, R. Iacocca, P.W. Lee, D. Madan, K. Moyer, H. Sanderow, *ASM Handbook Volume 07: Powder Metal Technologies and Applications*, ASM International, USA, 1998.
- [40] K.G. Prashanth, S. Scudino, T. Maity, J. Das, J. Eckert, Is the energy density a reliable parameter for materials synthesis by selective laser melting? *Mater. Res. Lett.* 5 (2017) 386–390, <https://doi.org/10.1080/21663831.2017.1299808>.
- [41] I. Shishkovsky, I. Yadroitsev, I. Smurov, Direct selective laser melting of nitinol powder, *Phys. Procedia* 39 (2012) 447–454, <https://doi.org/10.1016/j.phpro.2012.10.060>.
- [42] T. Bormann, R. Schumacher, B. Müller, M. Mertmann, M. de Wild, Tailoring selective laser melting process parameters for NiTi implants, *J. Mater. Eng. Perform.* 21 (2012) 2519–2524, <https://doi.org/10.1007/s11665-012-0318-9>.
- [43] T. Gustmann, A. Neves, U. Kühn, P. Gargarella, C.S. Kiminami, C. Bolfarini, J. Eckert, S. Pauly, Influence of processing parameters on the fabrication of a Cu-Al-Ni-Mn shape-memory alloy by selective laser melting, *Addit. Manuf.* 11 (2016) 23–31, <https://doi.org/10.1016/j.addma.2016.04.003>.
- [44] U. Gaitzsch, J. Drache, K. McDonald, P. Müller, P. Lindquist, Obtaining of Ni-Mn-Ga magnetic shape memory alloy by annealing electrochemically deposited Ga/Mn/Ni layers, *Thin Solid Films* 522 (2012) 171–174, <https://doi.org/10.1016/j.tsf.2012.08.019>.
- [45] K. Malukhin, K. Ehmann, Development of a monolithic shape memory alloy manipulator, in: S. Ratchev, S. Koelemeijer (Eds.), *Micro-Assem. Technol. Appl.*, Springer US, Boston, MA, 2008, pp. 243–250, [https://doi.org/10.1007/978-0-387-77405-3\\_23](https://doi.org/10.1007/978-0-387-77405-3_23).
- [46] H.-J. Lee, J.-G. Song, D.-G. Ahn, Investigation into the influence of feeding parameters on the formation of the fed-powder layer in a powder bed fusion (PBF) system, *Int. J. Precis. Eng. Manuf.* 18 (2017) 613–621, <https://doi.org/10.1007/s12541-017-0073-9>.
- [47] C. Kamath, B. El-dasher, G.F. Gallegos, W.E. King, A. Sisto, Density of additively-manufactured, 316L SS parts using laser powder-bed fusion at powers up to 400 W, *Int. J. Adv. Manuf. Technol.* 74 (2014) 65–78, <https://doi.org/10.1007/s00170-014-5954-9>.
- [48] B. Palumbo, F. Del Re, M. Martorelli, A. Lanzotti, P. Corrado, Tensile properties characterization of AlSi10Mg parts produced by direct metal laser sintering via nested effects modeling, *Materials* 10 (2017) 144, <https://doi.org/10.3390/ma10020144>.
- [49] N. Read, W. Wang, K. Essa, M.M. Attallah, Selective laser melting of AlSi10Mg alloy: process optimisation and mechanical properties development, *Mater. Des.* 65 (2015) 417–424, <https://doi.org/10.1016/j.matdes.2014.09.044> 1980–2015.
- [50] S. Tammas-Williams, P.J. Withers, I. Todd, P.B. Prangnell, Porosity regrowth during heat treatment of hot isostatically pressed additively manufactured titanium components, *Scr. Mater.* 122 (2016) 72–76, <https://doi.org/10.1016/j.scriptamat.2016.05.002>.
- [51] H.E. Exner, G. Petzow, A critical assessment of porosity coarsening during solid state sintering, *Adv. Sci. Technol.* 45 (2006) 539–548 doi:10.4028/www.scientific.net/AST.45.539.
- [52] M.A. Spears, A.G. Evans, Microstructure development during final/intermediate stage sintering—II. Grain and pore coarsening, *Acta Metall.* 30 (1982) 1281–1289, [https://doi.org/10.1016/0001-6160\(82\)90146-8](https://doi.org/10.1016/0001-6160(82)90146-8).
- [53] F.M.C. Nilsén, Processing and Properties of MSM Based Hybrid Materials, Doctoral

- dissertation Aalto University, 2018, <http://urn.fi/URN:ISBN:978-952-60-8099-4>.
- [54] M. Agarwala, D. Bourell, J. Beaman, H. Marcus, J. Barlow, Direct selective laser sintering of metals, *Rapid Prototyp. J.* 1 (1995) 26–36, <https://doi.org/10.1108/13552549510078113>.
- [55] O. Heczko, L. Straka, Compositional dependence of structure, magnetization and magnetic anisotropy in Ni–Mn–Ga magnetic shape memory alloys, *J. Magn. Magn. Mater.* 272–276 (2004) 2045–2046, <https://doi.org/10.1016/j.jmmm.2003.12.819>.
- [56] R. Wróblewski, M. Leonowicz, Effect of annealing conditions on the structure of Ni<sub>50</sub>Mn<sub>29</sub>Ga<sub>21</sub> shape memory alloy, *Solid State Phenom.* 154 (2009) 151–156 [doi:10.4028/www.scientific.net/SSP.154.151](https://doi.org/10.4028/www.scientific.net/SSP.154.151).
- [57] V. Sánchez-Alarcos, V. Recarte, J.I. Pérez-Landazábal, G.J. Cuello, Correlation between atomic order and the characteristics of the structural and magnetic transformations in Ni–Mn–Ga shape memory alloys, *Acta Mater.* 55 (2007) 3883–3889, <https://doi.org/10.1016/j.actamat.2007.03.001>.
- [58] B. Ingale, R. Gopalan, M. Rajasekhar, S. Ram, Studies on ordering temperature and martensite stabilization in Ni<sub>55</sub>Mn<sub>20</sub>–xGa<sub>25</sub>+x alloys, *J. Alloys Compd.* 475 (2009) 276–280, <https://doi.org/10.1016/j.jallcom.2008.08.004>.
- [59] M.F. Qian, X.X. Zhang, L.S. Wei, L. Geng, H.X. Peng, Effect of chemical ordering annealing on martensitic transformation and superelasticity in polycrystalline Ni–Mn–Ga microwires, *J. Alloys Compd.* 645 (2015) 335–343, <https://doi.org/10.1016/j.jallcom.2015.05.118>.
- [60] I. Flores Ituarte, O. Wiikinkoski, A. Jansson, Additive manufacturing of polypropylene: a screening design of experiment using laser-based powder bed fusion, *Polymers* 10 (2018) 1293, <https://doi.org/10.3390/polym10121293>.